Progress In Electromagnetics Research M, Vol. 140, 1–12, 2026

PIER M

(Received 25 June 2026, Accepted 2 August 2026, Scheduled 12 September 2026)

Wideband Low-Profile Circularly Polarized Crossed-Dipole Antenna Based on AMC Reflector

He Liu[1], Han Lin[1,*], Zhonggen Wang[1], and Wenyan Nie[2]

[1]School of Electrical and Information Engineering, Anhui University of Science and Technology, Huainan 232001, China
[2]School of Mechanical and Electrical Engineering, Huainan Normal University, Huainan 232001, China

ABSTRACT: This paper proposes a wideband, low-profile, circularly polarized (CP) crossed-dipole antenna with an artificial magnetic conductor (AMC) reflector. The antenna consists mainly of a pair of orthogonal half-wavelength dipoles, two 90° phase-delay rings, four parasitic patches, four pairs of vertically arranged metallic strips, an AMC reflector, and a square ground plane. CP radiation is generated by exciting bow-tie dipole arms via phase-delay rings. Introducing parasitic patches and vertical metallic strips optimizes the surface current distribution, broadening the impedance-matching bandwidth and axial ratio bandwidth (ARBW). Meanwhile, using the AMC structure as a reflector effectively reduces the antenna profile. We fabricate a prototype of the proposed antenna to verify consistency between simulated and measured results. The measured results show that impedance bandwidth (IBW) is 1.51–2.54 GHz (50.9%), and ARBW is 1.53–2.51 GHz (48.5%). The antenna achieves a peak gain of 8.5 dBic and an average gain of 7.05 dBic across the entire operating band. Furthermore, the antenna features an ultra-low profile of $0.12\lambda_L$ at the lowest operating frequency.

1. INTRODUCTION

In modern wireless communication systems, CP antennas have been widely adopted in various wireless terminals such as GPS and satellite communication devices due to prominent advantages in alleviating polarization mismatch and suppressing multipath fading [1]. Currently, the operating frequency bands for diverse wireless services keep increasing, while the reserved installation space for antennas in communication devices is continuously reduced. This puts forward the design requirements of wide bandwidth and low profile for antennas. Under such application scenarios, low-profile wideband CP antennas have become the optimal solution for multi-band communication equipment. Among them, CP crossed-dipole antennas have emerged as a major research focus in this field due to their simple feeding structure and inherent capability to realize circular polarization [2].

Nevertheless, traditional crossed-dipole antennas suffer from a single resonant mode and narrow CP bandwidth, which limits their practical applications in various scenarios [3]. To address bandwidth limitation and further extend the CP bandwidth of crossed-dipole antennas, researchers have proposed a variety of optimized configurations. In [4] and [5], parasitic magneto-electric dipoles and parasitic patches are adopted to achieve relative CP bandwidths of 28.6% and 33%, respectively. Feng et al. constructed a multi-mode resonance by employing an asymmetric cross-loop in [6], increasing the CP bandwidth to 53.4%. Similarly, when two types of parasitic patches are loaded as additional structures in [7], the antenna obtains an ARBW of up to 66%. Some designs can even integrate filtering functionality via parasitic patches [8]. Although above methods using extra parasitic structures can realize a wide ARBW, the introduced additional structures inevitably increase the antenna profile. Meanwhile, extra parasitic losses are generated, which degrade the radiation efficiency. In [9] and [10], inclined fences and shorting pins are introduced to broaden the CP bandwidth and create new current paths for profile reduction. The two antennas achieve ARBWs of 59.7% and 63.4%, respectively, yet both exhibit a low radiation gain below 5 dBic. A dual-cavity-backed structure is adopted for the crossed-dipole antenna in [11]. It delivers an ARBW of 66.7% and high gain, but its profile height reaches $0.25\lambda_L$ at the lowest operating frequency, resulting in a bulky profile. Subsequent studies further optimized dipole shapes based on cavity-backed structures. Multiple schemes, including circular rings [12], bow-tie dipoles [13], Y-shaped arms [14], modified L-shaped arms [15], and traveling-wave loops [16], have been adopted to expand the ARBW. Nevertheless, excessive profile height remains an inherent drawback of such cavity-backed antennas. To tackle the high-profile issue, AMC structures are used in [17–19] for low-profile design, compressing the antenna profile to approximately $0.1\lambda_L$ and effectively reducing the overall height. However, the antenna in [17] achieves only an ARBW of 39%, indicating unsatisfactory wideband performance. A comprehensive review of the existing literature reveals that current designs struggle to simultaneously achieve low profile, wide CP bandwidth, and high gain. Therefore, developing high-performance CP antennas that integrate all three favorable characteristics remains a formidable challenge.

To address the aforementioned challenges, this paper presents a low-profile circularly polarized (CP) crossed-dipole antenna incorporating a coin-shaped AMC reflector. Asymmetric dipole arms and parasitic patches are strategically

* Corresponding author: Han Lin (hanlin@aust.edu.cn).

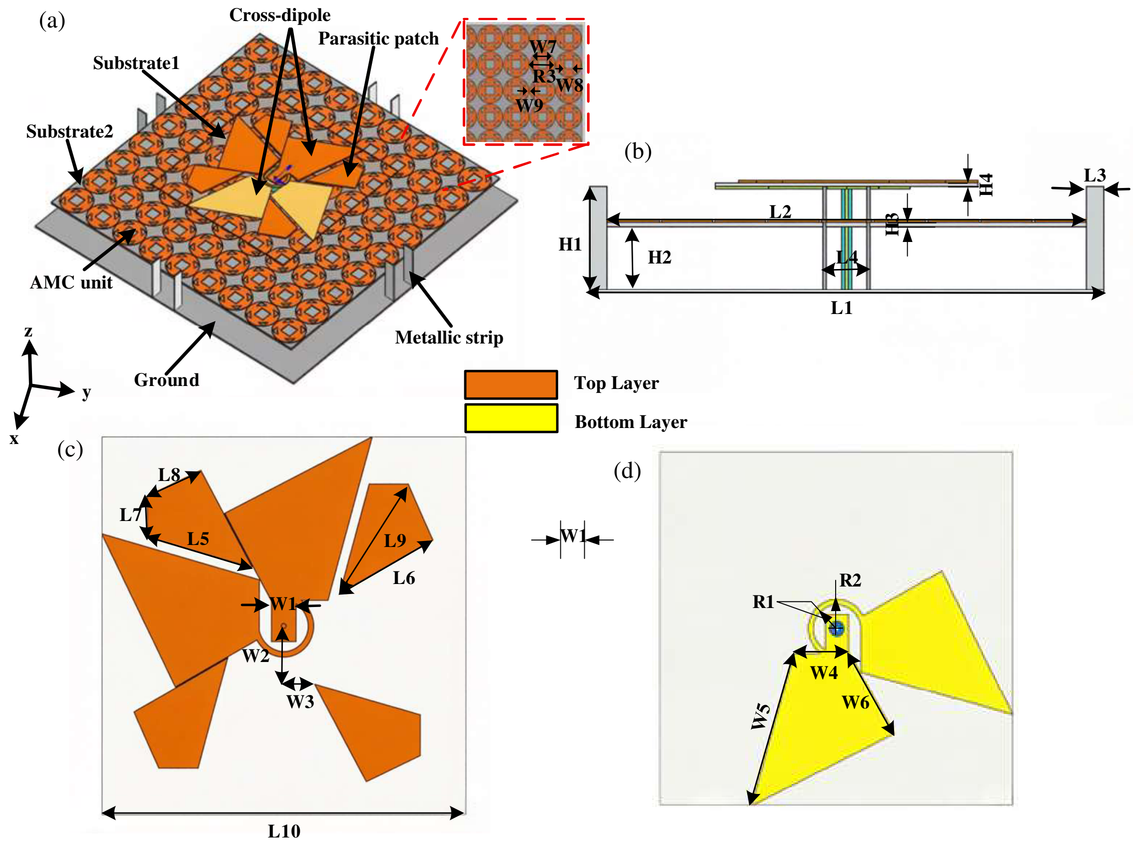

FIGURE 1. Configuration of the proposed antenna. (a) 3-D view, (b) side view, (c) dipole antenna layer top side, and (d) dipole antenna layer bottom side.

employed to excite additional resonant modes, effectively expanding the 3-dB ARBW. By leveraging the in-phase reflection property of AMC unit cells, the antenna profile is significantly reduced to $0.12\lambda_L$. Crucially, multiple metallic strips are arranged around the ground plane to perturb the surface current distribution. This configuration mitigates undesirable asymmetrical coupling between the AMC reflector and dipole elements, further optimizing axial ratio performance across the operating band. Benefiting from this synergistic design strategy, the proposed antenna achieves a wide overlapping bandwidth (OBW) of 48.5%, with a peak gain of 8.5 dBic and an average gain of 7.05 dBic. Combining an ultra-low profile with high gain and wideband CP performance, the proposed antenna demonstrates significant potential for GPS receivers and satellite communication terminals. For cost considerations, FR4 substrates are adopted for all antenna substrates.

2. ANTENNA DESIGN

2.1. Antenna Configuration

As shown in Fig. 1, the proposed antenna consists mainly of a pair of orthogonal half-wavelength dipoles, two 90° phase-delay rings, four parasitic patches, four pairs of vertically arranged metallic strips, an AMC plate, and a square ground plane. The radiating elements are etched on an FR4 substrate with a dimension of $74\times74\times0.8\,\mathrm{mm}^3$ ($\varepsilon_r = 4.4$, $\tan\delta = 0.02$). The orthogonal half-wavelength dipoles printed on the upper and lower surfaces of the dielectric substrate, together with phase-delay rings, form the antenna's main radiating part. Four identical parasitic patches are etched between the asymmetric bow-tie dipole arms. To realize the low-profile characteristic, periodically arranged AMC units are loaded on the top surface of another 1 mm-thick FR4 substrate. Moreover, four pairs of metallic strips are deployed along the edges of the ground plane to improve the axial ratio performance. A $50\,\Omega$ coaxial cable is adopted for feeding. Its inner and outer conductors are connected to the dipole arms on the upper and lower layers of the dielectric substrate, respectively, so as to radiate circularly polarized electromagnetic waves. Table 1 provides the antenna's dimensional parameters.

2.2. Antenna Design Process

Figure 2 illustrates the design evolution of the proposed antenna. Antenna I uses only two pairs of cross-shaped basic bow-tie dipoles connected by 90° phase-delay rings as its radiating elements. On the basis of Antenna I, Antenna II is modified to employ asymmetric crossed bow-tie dipoles. Four quadrilateral parasitic patches are etched around the crossed dipoles to form Antenna III. An AMC reflector is installed between the ground plane and radiating elements for Antenna IV. For Antenna V,

TABLE 1. Comparison of the proposed antenna with several existing antennas.

Parameter	$L1$	$L2$	$L3$	$L4$	$L5$	$L6$	$L7$	$L8$	$L9$	$L10$
Value (mm)	145	135	5	10	22.5	21.5	8	12	25.5	74
Parameter	$W1$	$W2$	$W3$	$W4$	$W5$	$W6$	$W7$	$W8$	$W9$	$R1$
Value (mm)	5	12	7.5	11.5	33	19.5	10	5	0.5	5
Parameter	$R2$	$R3$	$H1$	$H2$	$H3$	$H4$				
Value (mm)	6.1	14.5	24	15	1	0.8				

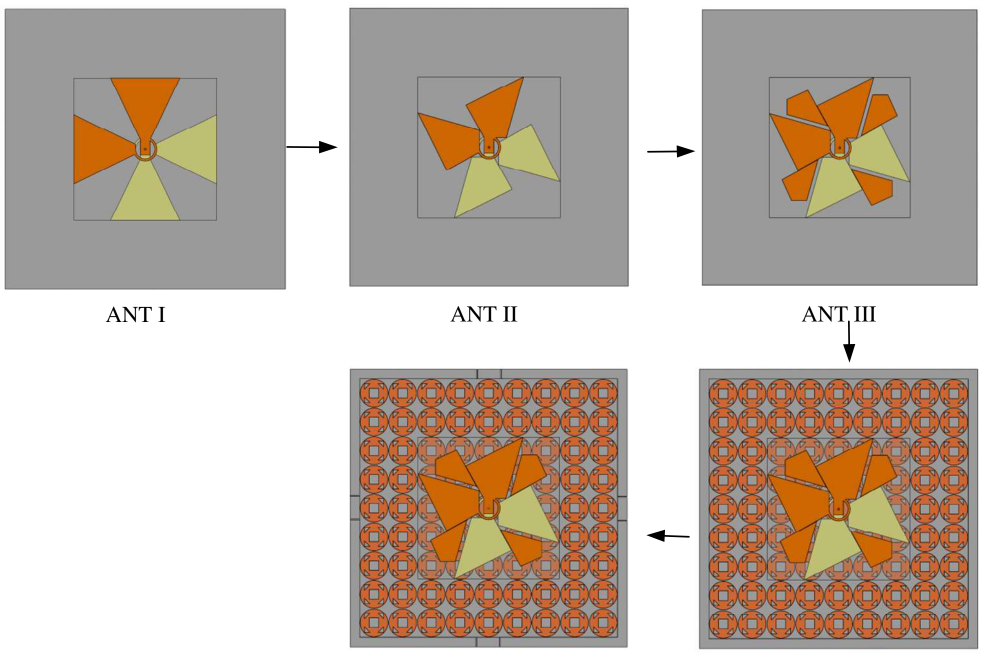

FIGURE 2. Design steps of the proposed antenna.

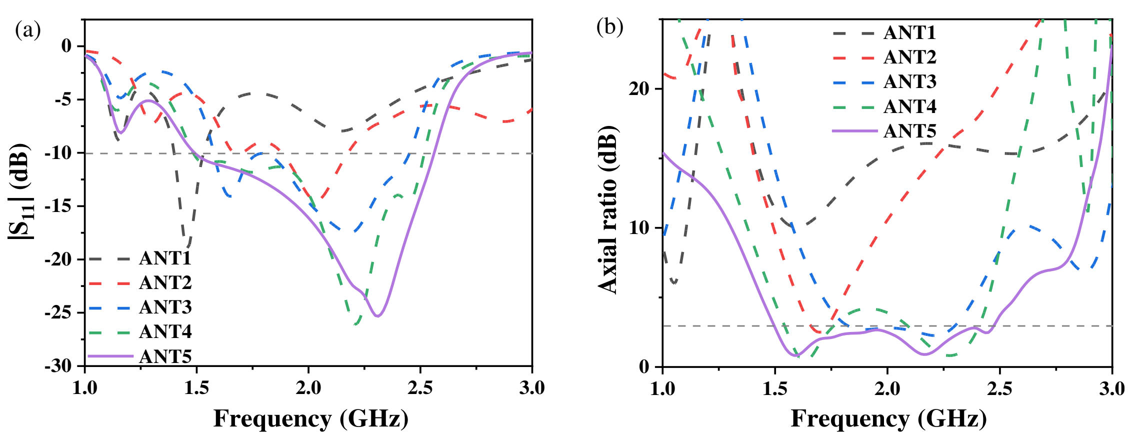

FIGURE 3. Simulated results of different antennas. (a) Impedance bandwidth and (b) axial ratio.

four pairs of metallic strips are arranged along the edges of the metal ground plane.

Figure 3 plots reflection coefficients and axial ratio curves of the five antennas. Antenna I employs a pair of orthogonal basic bow-tie dipoles printed on the upper and lower surfaces of an FR4 dielectric substrate, which has a relative permittivity ε_r of 4.4 and a loss tangent $\tan\delta$ of 0.02. The initial arm length of each dipole is set to half-wavelength corresponding to the target center frequency. The flare angle of the bow-tie dipole is optimized via parametric simulation to achieve balanced impedance matching. The radius of the 90° phase-delay loop is designed to introduce the required 90° phase differ-

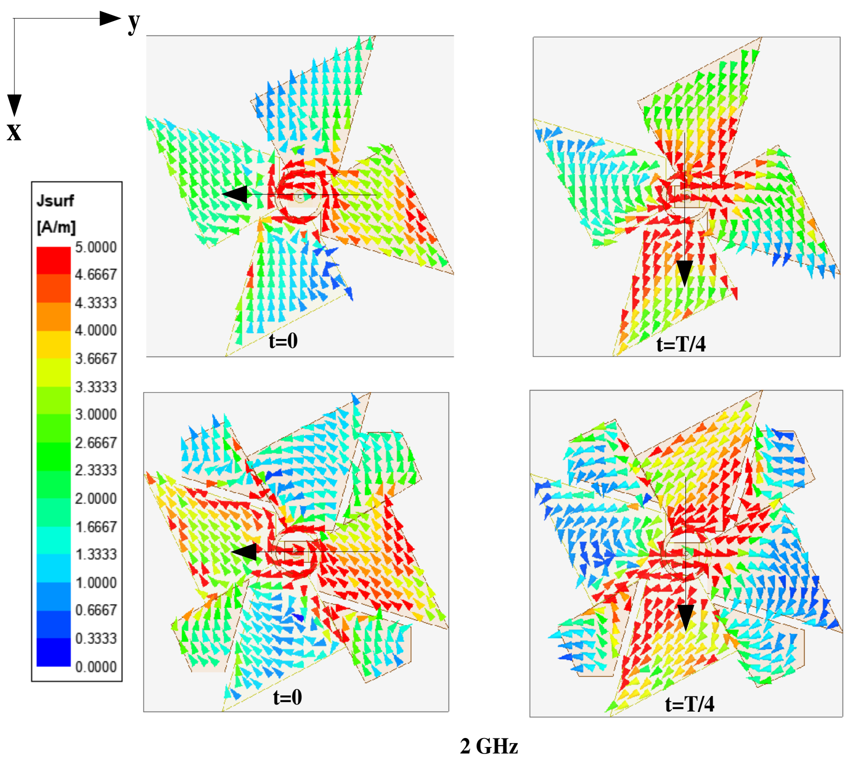

FIGURE 4. Surface current distributions before and after loading parasitic patches.

ence between the two orthogonal dipoles, which serves as the fundamental condition for generating circular polarization. It achieves a -10 dB IBW ranging from 1.39 to 1.53 GHz, with the axial ratio exceeding 10 dB across the entire band. Although it exhibits a tendency for circular polarization, the antenna suffers from insufficient bandwidth and poor polarization performance.

Based on Antenna I, Antenna II adopts an asymmetric crossed bow-tie dipole structure, with lengths of the dipole arms optimized to 33 mm and 19.5 mm, respectively. This asymmetry introduces additional resonant modes near the original resonant frequency of the dipoles, effectively broadening the impedance bandwidth. A parametric sweep over the length difference between dipole arms is carried out to maximize the overlapping range of the impedance bandwidth and potential axial-ratio bandwidth, laying a foundation for the subsequent optimization of circular polarization performance. By adjusting the lengths of asymmetric dipole arms, the IBW shifts towards higher frequencies and is broadened to 1.88–2.17 GHz. Meanwhile, new effective axial-ratio resonant points are generated, which address the lack of circular-polarization capability in Antenna I.

To further broaden the bandwidth and improve impedance matching, as well as axial ratio characteristics, four identical parasitic patches are etched in gaps between adjacent arms of asymmetric bow-tie dipoles to achieve strong near-field electromagnetic coupling. The length of each parasitic patch is approximately 0.3 times the wavelength, corresponding to the center frequency. After simulation optimization, these patches extend the effective current path of the radiating structure and introduce additional resonant modes for bandwidth enhancement. Fig. 4 presents the antenna's surface current distributions at 2 GHz. Without parasitic patches, surface currents are mainly concentrated on the dipole arms with a limited distribution range. The amplitude and phase of orthogonal components are unbalanced, which restricts ARBW. After introducing parasitic patches, strong induced currents are excited on the patches via near-field electromagnetic coupling. These induced currents are superimposed on the dipoles' original currents, which greatly extends effective current paths and renders the current distribution more uniform and symmetric [14]. In the figure, the currents spread over not only the original dipole arms but also the parasitic patches, forming an extensive current network. Accordingly, the antenna's -10 dB IBW is expanded to 1.57–2.44 GHz, and the 3 dB ARBW is extended to 1.83–2.29 GHz.

To reduce the antenna profile, an AMC reflector is inserted between the radiating elements and the ground plane of Antenna III to develop Antenna IV. The proposed coin-shaped AMC unit consists of a slotted circular patch on a thin FR4 layer backed by an air gap and a ground plane. Within 1.36–2.57 GHz, its reflection phase stays between 90° and +90°, meaning that it acts as an in-phase reflector instead of a conventional perfectly electrically conducting (PEC) ground. This property permits the radiator-to-ground distance to shrink to approximately $0.12\lambda_L$ while still maintaining constructive interference for CP radiation. Section 2.4 provides this AMC's detailed equivalent-circuit model and parametric analysis. The -10 dB IBW is further extended to 1.49–2.51 GHz, and a new low-frequency band of 1.54–1.75 GHz is added to the ARBW,

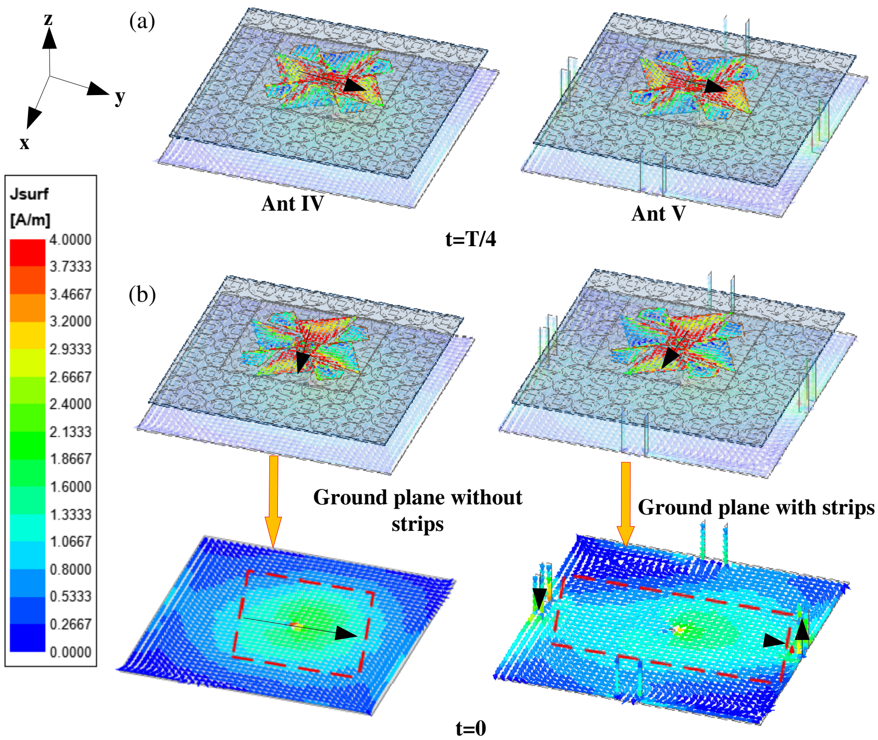

FIGURE 5. Surface current distributions at 1.6 GHz. (a) $t = T/4$, (b) $t = 0$.

leading to a remarkable improvement in CP performance. Nevertheless, affected by the electromagnetic coupling between the AMC structure and radiating elements, the CP characteristics degrade around 2 GHz, and the antenna operates in elliptical polarization state within this frequency range.

To address the axial ratio deterioration of Antenna IV, four pairs of metallic strips are symmetrically arranged along the edges of the ground plane in Antenna V. Fig. 5 depicts the surface current distributions of Antenna IV and Antenna V at 1.6 GHz for analyzing the effects of the metallic strips. At $t = T/4$, resultant currents of both antennas flow along the $+y$ direction. At $t = 0$, Antenna IV features dominant currents along the $+x$ direction. Strong induced currents along the $+y$ direction emerge on dipoles due to coupling with the AMC reflector. This degrades the axial ratio at low frequencies. Compared with the current distribution on the ground plane of Antenna IV, the adopted metallic strips extend the current paths along the $+y$ axis and effectively suppress the undesired currents on the y-axis [20]. At $t = 0$, the resultant current is redirected toward the $+x$ direction after this optimization, which improves axial ratio performance and realizes right-handed circular polarization (RHCP) radiation. The incorporated metallic strips introduce an additional current path that perturbs the surface current distribution along the dipoles. This perturbation effectively compensates for the asymmetrical coupling induced by the AMC reflector, mitigating axial-ratio degradation at lower frequencies and broadening the overall AR bandwidth. The -10 dB IBW extends from 1.49 to 2.56 GHz, and the ARBW covers 1.50–2.47 GHz. The antenna achieves stable CP across the entire operating band, combining low profile and wide bandwidth.

2.3. Operating Principle of Circular Polarization

To analyze CP radiation characteristics of the final antenna prototype, Fig. 6 presents surface current distributions at 1.6 GHz, 2.1 GHz, and 2.4 GHz. The currents are mainly distributed on the crossed dipoles and rotate counterclockwise from $t = 0$ to $t = T/4$. Vertical and horizontal current components have equal amplitudes and orthogonal phases, which ensure stable CP radiation at central frequency points.

At 2.4 GHz, the current distribution differs from that at lower frequencies. The current direction undergoes a slight oblique deflection and flows obliquely along the dipole arms instead of strictly along the vertical or horizontal directions. Despite a minor deviation in current orientation, the two orthogonal current components still maintain sufficient amplitude and a stable phase difference, thus retaining favorable CP radiation performance.

Combining current distributions at the three frequency points, the antenna's surface currents rotate counterclockwise along the $+z$ axis within the operating band. According to the right-hand rule, the proposed final antenna radiates RHCP waves.

2.4. Design and Working Principle of the AMC Structure

Unlike a conventional perfect electric conductor (PEC) ground plane, which requires a radiator-to-ground spacing of $\lambda/4$, the proposed coin-shaped AMC unit has an in-phase reflection characteristic (phase within $\pm 90°$) across 1.36–2.57 GHz, enabling a reduced profile of $0.12\lambda_L$.

As illustrated in Fig. 7(a), the unit features a circular patch with four triangular slots and one rectangular slot, fabricated on

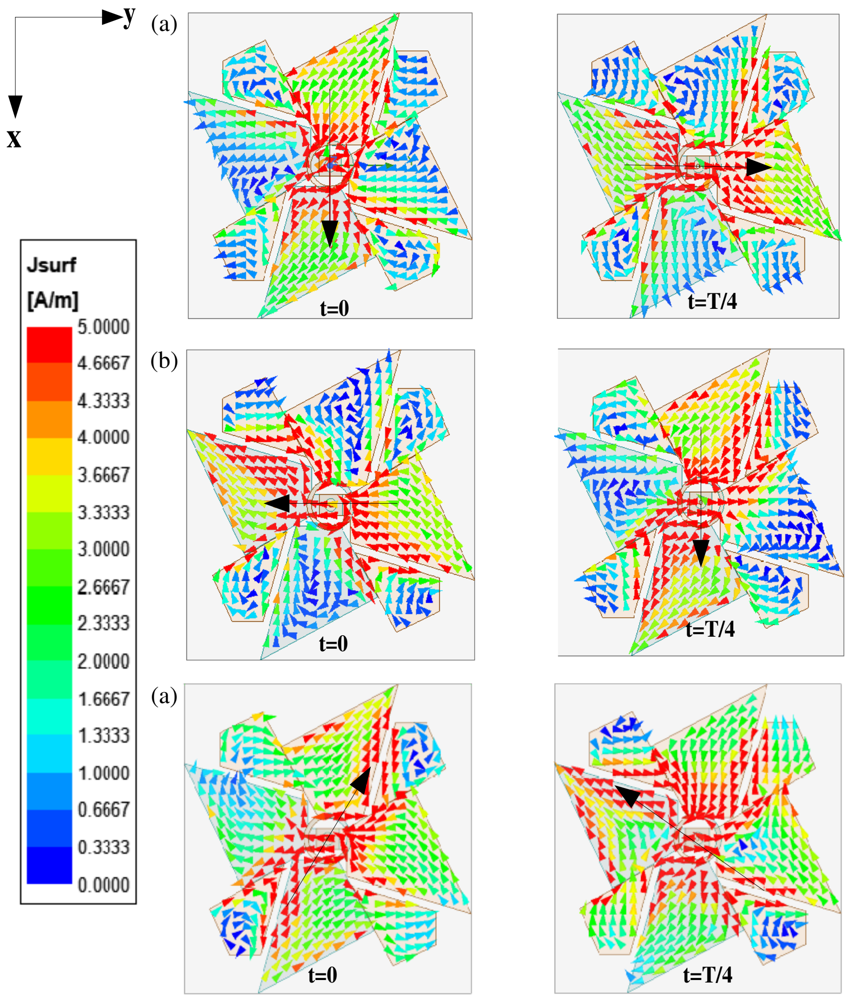

FIGURE 6. Surface current distribution at (a) 1.6 GHz, (b) 2.1 GHz, and (c) 2.4 GHz.

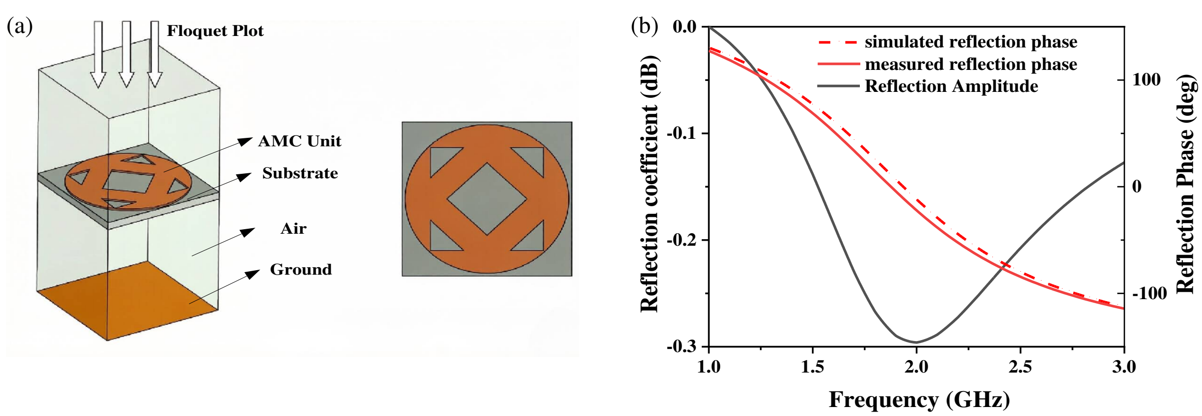

FIGURE 7. Configuration and results of the AMC unit. (a) Structure of the AMC unit and (b) simulated and measured results.

a 1-mm FR4 substrate. To validate the simulated performance, we fabricate and characterize a standalone AMC unit in an anechoic chamber using a vector network analyzer. As plotted in Fig. 7(b), the measured in-phase reflection band ranges from 1.33 to 2.52 GHz (62% fractional bandwidth), closely aligning with the simulation. The slight frequency offset is primarily attributed to FR4 dielectric tolerances and residual edge effects inherent in the single-unit measurement setup. Nevertheless, the reflection magnitude remains below -0.3 dB within this band, indicating near-perfect reflection [21]. This confirms that the 9×9 array deployed in the final antenna design retains robust in-phase reflection while minimizing edge disturbances.

To explain the operating principle of the AMC unit, Fig. 8 presents the equivalent circuit of the AMC reflector. The gaps

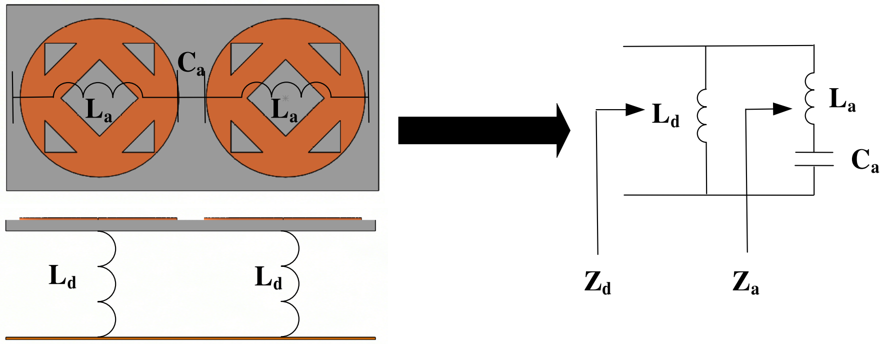

FIGURE 8. Equivalent circuit model of the AMC reflector.

between periodically arranged AMC metal patches produce capacitance C_a. The metallic patches of the AMC unit form inductance L_a, and the air layer between the ground reflector and AMC patches contributes to inductance L_d [22].

The total surface impedance (η) is expressed as follows:

$$\eta = Z_a // Z_d = jL_d\omega \frac{1 - \omega^2 L_d C_a}{1 - (L_d + L_a) C_a} \tag{1}$$

where Z_a and Z_d denote the equivalent impedances of the patch and grounded substrate, respectively; ω represents the angular frequency; L_a and C_a are the equivalent inductance and capacitance of the metallic patch; L_d stands for the equivalent inductance of the dielectric grounded section. According to Equation (1), the resonant frequency f_a and reflection phase φ of the AMC unit can be calculated by the following formulas:

$$f_a = \frac{1}{2\pi (L_d + L_a) C_a} \tag{2}$$

$$j\varphi = \ln \Gamma = \frac{\eta - \eta_0}{\eta + \eta_0} \tag{3}$$

where η_0 refers to the intrinsic wave impedance of free space, and Γ denotes the Fresnel reflection coefficient for normal incidence of plane waves. Equations (2) and (3) clearly illustrate the effects of various parameters on the resonant frequency and reflection coefficient of the AMC unit. By adjusting parameters such as dielectric material, dimensions of metal patches, and height of the air layer, the desired L_C parallel resonance can be achieved to obtain the in-phase reflection bandwidth within the target frequency band. To investigate the parameter influence on the AMC performance, parametric simulations are carried out. Only one variable is changed each time while all others remain constant. Figs. 9(a) and 9(b) show the effects of the diameter $R3$ of the coin-shaped patch and the air layer height $H2$ on the reflection phase of the proposed AMC unit. It is obvious that $R3$ and $H2$ greatly affect the in-phase reflection range of the AMC reflector. As $R3$ increases from 14 mm to 15 mm, the in-phase reflection band shifts toward lower frequencies. Similarly, when $H2$ rises from 14 mm to 16 mm, the frequency band corresponding to the reflection phase between 90° and +90° also moves downward. Accordingly, modifying $R3$ and $H2$ can tune the resonant frequency and in-phase reflection bandwidth to meet design specifications.

To investigate the influence of the air-layer height of the AMC reflector on the antenna's reflection coefficient and axial ratio, Figs. 9(c) and 9(d) present the analysis of the reflection coefficient and axial ratio with respect to $H2$. As evident from the figures, increasing the air gap height ($H2$) from 13 mm to 17 mm maintains a stable impedance bandwidth ($\sim$ 49–52%) but induces a sharp non-monotonic shift in the AR response. $H2 = 15$ mm yields the widest 3-dB AR bandwidth, whereas $H2 = 17$ mm collapses this bandwidth due to disrupted phase synchronicity. Thus, 15 mm is selected to maximize the overlapping bandwidth.

To quantitatively determine the optimal array size, the empirical boundary criterion for finite AMC arrays is adopted to constrain edge-induced phase deviation. The theoretical minimum N is derived as follows:

$$N \geq \frac{\lambda_{\max}}{2p} \tag{4}$$

where $\lambda_{\max} = 221$ mm corresponds to the lower boundary of the $\pm 90°$ in-phase reflection band ($f_{\min} = 1.36$ GHz), and $p = 15$ mm is the periodicity of the unit cell. Substituting these values yields $N > 7.37$, indicating that the theoretical minimum integer N is 8.

Full-wave simulations of the integrated antenna system are carried out to verify this boundary condition. As illustrated in Fig. 10, reducing the array scale to 7×7 ($N = 7$) leads to degraded axial ratio and insufficient impedance matching at 1.5 GHz, failing to meet the design criteria. In contrast, the 9×9 configuration achieves favorable impedance bandwidth and axial ratio bandwidth at the same frequency. The 9×9 array provides sufficient margin relative to the theoretical limit, effectively suppressing edge diffraction and forming a sufficiently large in-phase reflection region for the crossed-dipole radiator. Accordingly, $N = 9$ is adopted in the final design.

To quantitatively demonstrate the advantages of the AMC reflector, Fig. 11 compares the simulated S_{11}, axial ratio, gain, and radiation efficiency between the proposed AMC-based antenna and a reference antenna with a PEC ground plane (with the identical 15 mm air spacing and additional metal strips). The two configurations achieve similar impedance bandwidths. Nevertheless, the PEC reference antenna has an axial ratio higher than 3 dB across most of the frequency band, resulting

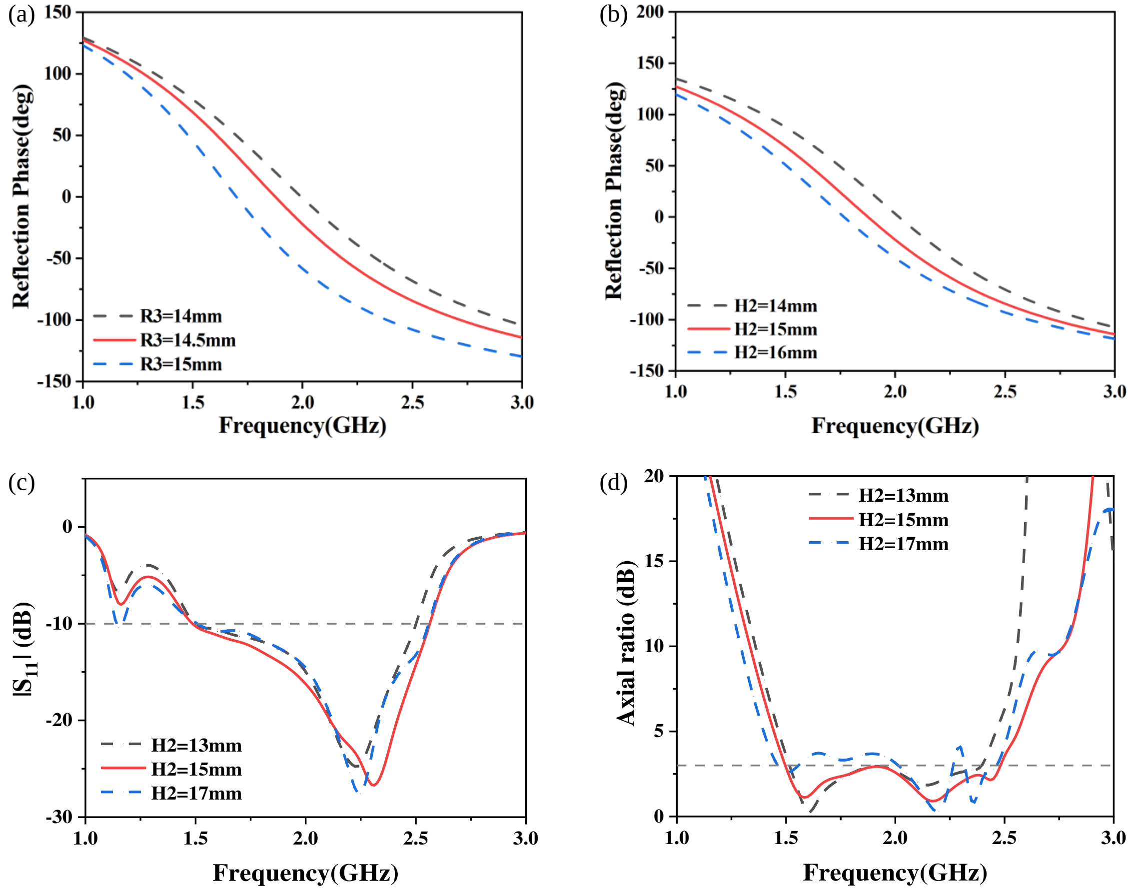

FIGURE 9. Parametric analysis of the AMC unit cell and the overall antenna. (a) Influence of R on reflection phase, (b) influence of H on reflection phase, (c) influence of $H2$ on Impedance bandwidth, and (d) influence of $H2$ on axial ratio.

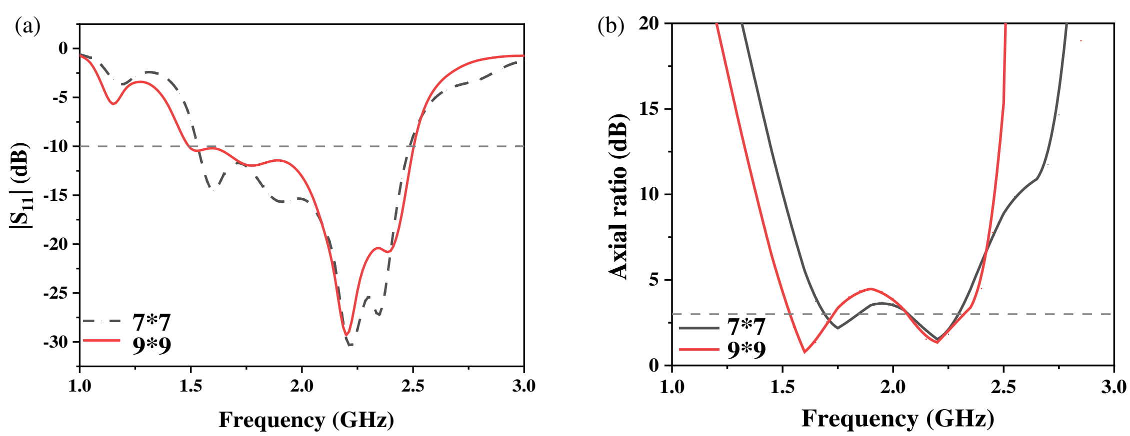

FIGURE 10. Simulated results of the antenna loaded with 7×7 and 9×9 AMC reflectors: (a) impedance bandwidth and (b) axial ratio.

in a narrow circular-polarization bandwidth. In contrast, the AMC-based antenna attains a 3-dB axial ratio bandwidth of 48.1% ranging from 1.50 to 2.47 GHz. Within this circularly polarized operating band, the AMC antenna maintains a gain of 5.8–8.5 dBic and a radiation efficiency exceeding 85%. Although the PEC antenna delivers higher gain at upper frequencies, such performance corresponds to linear polarization; severe destructive interference will occur if it is forced to operate under circular polarization conditions. The slight gain drop observed for the AMC antenna at high frequencies mainly stems from the deviation of the AMC reflection phase away from 0° near the band edge and increased surface wave loss. This tradeoff is acceptable given that the profile is compressed from $\lambda/4$ down to $0.12\lambda_L$.

3. MEASUREMENT AND COMPARISON

A prototype antenna is fabricated using printed circuit technology to verify the feasibility of the proposed design. Fig. 12

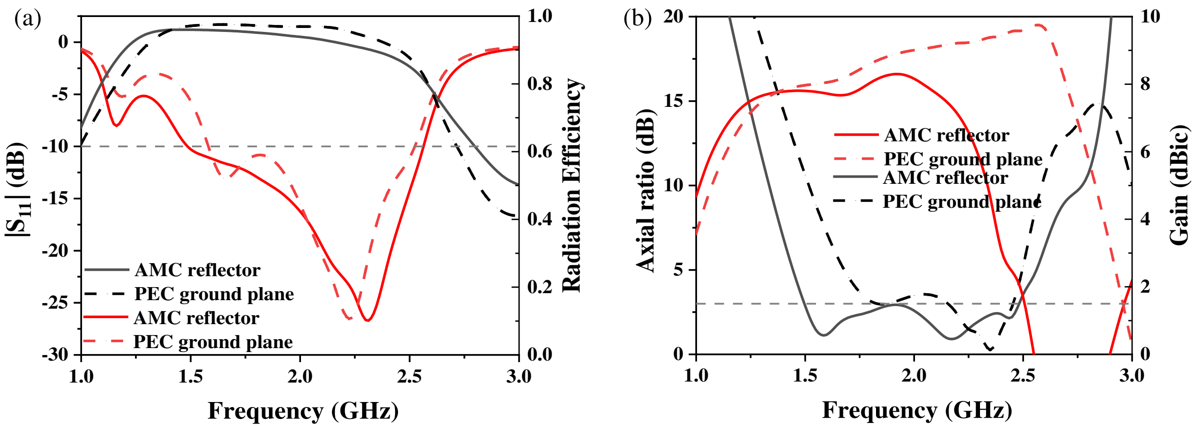

FIGURE 11. Simulated comparison of the antenna with AMC reflector and PEC ground plane, (a) impedance bandwidth and radiation efficiency, and (b) axial ratio and gain.

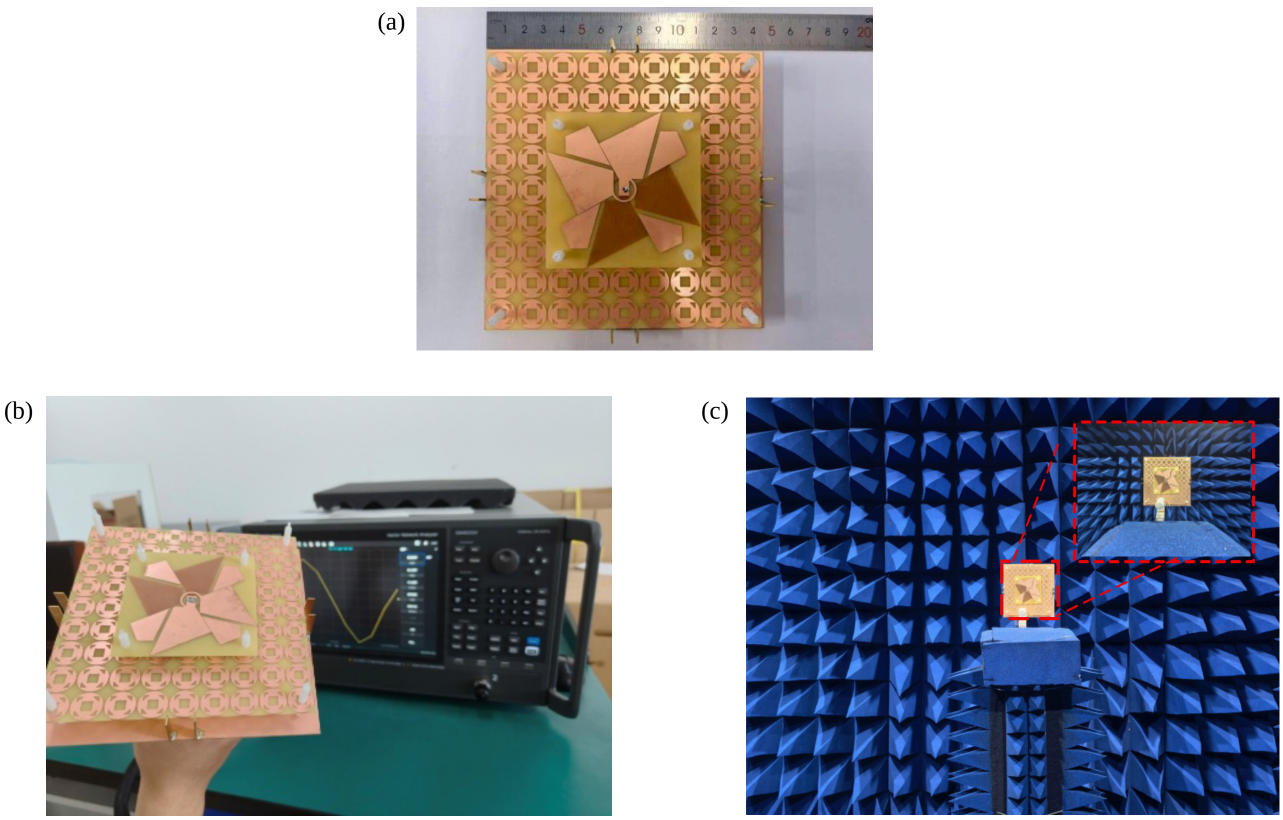

FIGURE 12. Antenna prototype and measurement environment. (a) Antenna prototype, (b) reflection coefficient measurement setup, and (c) measurement setup.

shows the manufactured prototype and the far-field measurement setup inside an anechoic chamber. A vector network analyzer (VNA) is first used to measure the impedance-matching performance, and far-field experiments are subsequently performed to characterize antenna radiation characteristics. FR4 substrates for the main radiator, AMC reflector, and bottom ground plane are assembled with nylon support pillars to ensure structural flatness. The antenna is excited by a 50 Ω coaxial cable, which connects to the VNA for impedance testing and to the measurement receiver for radiation-pattern acquisition.

The axial ratio, gain, and radiation patterns are measured in a far-field anechoic chamber, while the impedance bandwidth is characterized via the VNA. Fig. 13 provides a comparison between simulated and measured results. As observed in Fig. 13(a), measured and simulated impedance bandwidths are 50.9% (1.51–2.54 GHz) and 52.84% (1.49–2.56 GHz), respectively. Fig. 13(a) also plots the simulated radiation efficiency against the left vertical axis; it stays above 85% over the operating band and slightly declines at high frequencies. Fig. 13(b) illustrates the simulated and measured axial ratio

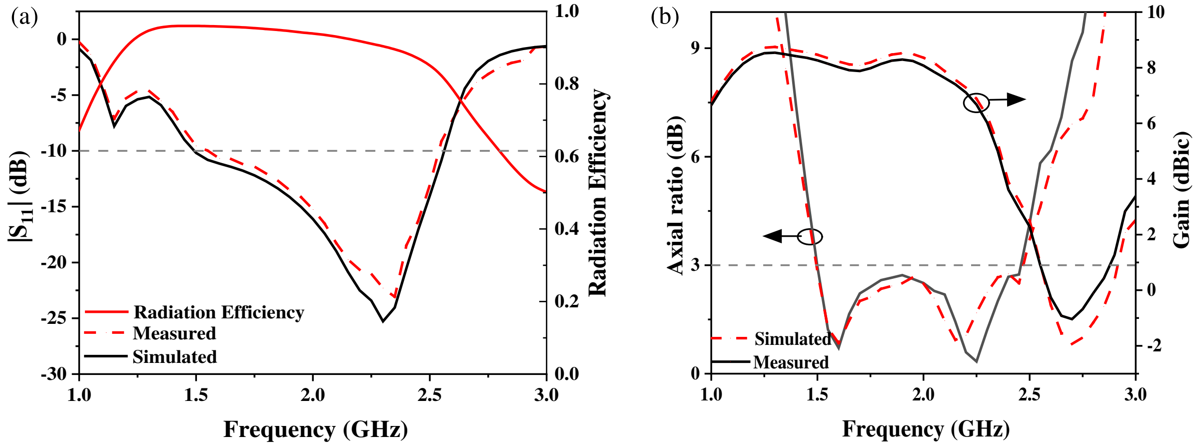

FIGURE 13. Comparison between measured and simulated curves. (a) Impedance bandwidth and radiation efficiency, and (b) axial ratio and gain.

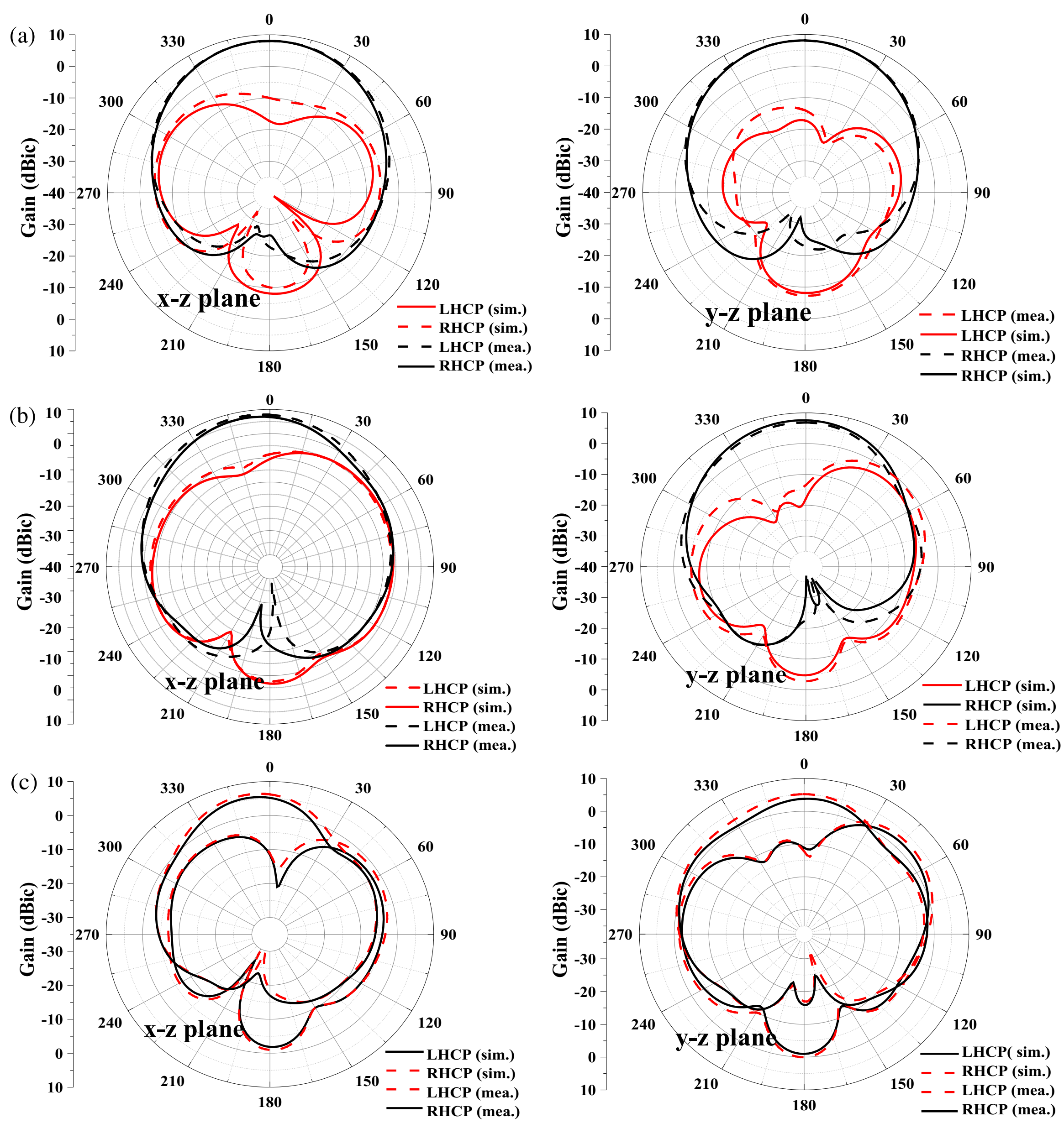

FIGURE 14. Simulated and measured radiation patterns of the antenna in both x-z and y-z planes at different frequencies. (a) 1.6 GHz, (b) 2.1 GHz, and (c) 2.4 GHz.

TABLE 2. Comparison of the proposed antenna with several existing antennas.

Ref.	Size (λ_L^3)	IBW (%)	ARBW (%)	OBW (%)	Peak gain (dBic)
[5]	$0.95 \times 0.95 \times 0.22$	57%	33%	33%	8.7
[7]	$0.62 \times 0.62 \times 0.15$	77.6%	66%	66%	8.4
[8]	$0.56 \times 0.56 \times 0.2$	71.8%	46.8%	46.8%	7.7
[9]	$0.22 \times 0.22 \times 0.13$	59.7%	61.5%	59.7%	3.9
[15]	$0.42 \times 0.43 \times 0.16$	61.3%	52.6%	52.6%	7.8
[17]	$0.93 \times 0.93 \times 0.1$	55.1%	39.0%	39.0%	8.4
This work	$0.73 \times 0.73 \times 0.12$	50.9%	48.5%	48.5%	8.5

and gain curves. The measured and simulated 3-dB axial ratio bandwidths are 48.51% (1.53–2.51 GHz) and 48.87% (1.50–2.47 GHz). The consistent trend between the efficiency degradation in Fig. 13(a) and the gain drop in Fig. 13(b) demonstrates that high-frequency performance deterioration mainly originates from increased ohmic and surface wave losses in the AMC structure, instead of measurement errors.

The measured operating band shifts slightly toward higher frequencies compared with the simulation, which is mainly attributed to fabrication tolerances. The primary factor is manual assembly of the 15 mm air layer. Minor height deviations (± 0.1 mm) are introduced, and fastening nylon standoffs inevitably cause shifts in the AMC resonant frequency. Besides, inherent variations in the relative permittivity of FR4 and edge diffraction induced by the finite 9×9 array collectively result in discrepancies from ideal infinite periodic simulation data. Meanwhile, the measured gain is in good agreement with simulations. The antenna achieves a peak gain of 8.5 dBic and an average gain of 7.05 dBic.

Figure 14 plots measured and simulated radiation patterns on the two principal planes (x-z and y-z planes) at 1.45 GHz, 2 GHz, and 2.4 GHz. The measured results show good consistency with the simulations. Notably, along the $+z$ (boresight) direction, the RHCP amplitude is at least 15 dB higher than that of the LHCP across all tested frequencies, confirming a cross-polarization level better than -15 dB and verifying high-quality RHCP radiation. However, slight asymmetries are observed between the $+z$ and $-z$ directions, primarily due to edge diffraction from the finite AMC array and minor structural perturbations from the feeding network. Consistent with efficiency trends in Fig. 13(a), a slight gain degradation is also noted at the higher end of the operating band, which is attributed to increased ohmic and surface-wave losses within the AMC structure at elevated frequencies.

To highlight the novelty of the proposed antenna, Table 2 summarizes the performance comparison with recently reported similar antennas [5, 7–9, 15, 17]. Compared with Ref. [5], the proposed design demonstrates a clear advantage in compact size, wider CP bandwidth, and higher peak gain. Furthermore, it exhibits a wider CP bandwidth and higher gain than the antennas in [8] and [17]. Although the CP bandwidth is slightly narrower than those in Refs. [7, 9], and [15], the proposed antenna achieves a significantly lower profile of $0.12\lambda_L$. This performance balance is largely attributed to using the AMC reflector, which favors a low-profile configuration suitable for conformal integration, albeit with a slight reduction in bandwidth compared to conventional high-gain designs.

4. CONCLUSION

In this paper, a wideband low-profile CP crossed-dipole antenna based on an AMC reflector is proposed. Parasitic patches are etched between the arms of asymmetric bow-tie dipoles to extend the surface-current path, and four pairs of vertical metal strips are loaded at the edges of the ground plane to suppress the coupled current between the dipole arms and the AMC structure. Combined with the AMC reflector, the profile height of the proposed antenna is successfully reduced to $0.12\lambda_L$. Measured results demonstrate that the -10 dB impedance bandwidth and 3 dB ARBW of the antenna cover 1.51–2.54 GHz (50.9%) and 1.53–2.51 GHz (48.5%), respectively, with an overlapping bandwidth of 48.5%. A peak gain of 8.5 dBic is achieved within the operating bandwidth, alongside stable radiation patterns. Benefiting from its ultra-low profile $(0.12\lambda_L)$, light weight, and wideband circular polarization performance, the proposed antenna is an ideal candidate for applications such as Global Positioning System (GPS) and compact satellite communication terminals, where space saving is critical. The current limitation lies in moderate peak average gain caused by ohmic and surface wave losses within the AMC structure, as well as the enlarged aperture of the 9×9 array. Future research will focus on improving the gain by adopting optimized metasurface covers and developing single-layer AMC configurations to reduce the transverse dimension.

ACKNOWLEDGEMENT

This work was supported in part by the Natural Science Research Project of Anhui Educational Committee under Grant No. 2025AHGXZK31006, in part by the Research Foundation of Jiangsu Engineering Research Center for Bionics Control Technology and Equipment under No. FSKZ202503, in part by the Anhui International Joint Research Center for Ancient Architecture Intelligence and Multi-Dimensional Modeling under No. GJZZX2025KF01, in part by the Anhui Provincial Natural Science Foundation of China under No. ZX20250143, in part by the Fujian Provincial Natural Science Foundation of China under No. 2024J08368.

REFERENCES

[1] Tu, Z.-H., K.-G. Jia, and Y.-Y. Liu, "A differentially fed wideband circularly polarized antenna," *IEEE Antennas and Wireless Propagation Letters*, Vol. 17, No. 5, 861–864, 2018.

[2] Kedze, K. E., H. Wang, Y. Kim, and I. Park, "Design of a reduced-size crossed-dipole antenna," *IEEE Transactions on Antennas and Propagation*, Vol. 69, No. 2, 689–697, 2021.

[3] Xue, F., Y. Zhang, J. Li, and H. Liu, "Circularly polarized cross-dipole antenna for UHF RFID readers applicated in the warehouse environment," *IEEE Access*, Vol. 11, 38 657–38 664, 2023.

[4] Ta, S. X. and I. Park, "Crossed dipole loaded with magneto-electric dipole for wideband and wide-beam circularly polarized radiation," *IEEE Antennas and Wireless Propagation Letters*, Vol. 14, 358–361, 2015.

[5] Sefidi, M., C. Ghobadi, J. Nourinia, and R. Naderali, "Broadband circularly polarized printed crossed-dipole antenna and its arrays for cellular base stations," *IEEE Access*, Vol. 12, 6842–6851, 2024.

[6] Feng, G., L. Chen, X. Xue, and X. Shi, "Broadband circularly polarized crossed-dipole antenna with a single asymmetrical cross-loop," *IEEE Antennas and Wireless Propagation Letters*, Vol. 16, 3184–3187, 2017.

[7] Wang, L., W.-X. Fang, Y.-F. En, Y. Huang, W.-H. Shao, and B. Yao, "Wideband circularly polarized cross-dipole antenna with parasitic elements," *IEEE Access*, Vol. 7, 35 097–35 102, 2019.

[8] Yang, H., Y. Liu, X. Li, X. Xiao, Z. Guo, Y. Zhang, X. Zhang, C. Wang, Y. Fang, C. Ye, and S. Wang, "A wideband circularly polarized filtering antenna using SRR and parasitic patch," *IEEE Antennas and Wireless Propagation Letters*, Vol. 24, No. 8, 2227–2231, 2025.

[9] Wu, R., J.-H. Lin, G.-H. Wen, S.-T. Cai, and F.-C. Chen, "A compact broadband circularly polarized antenna with novel tilt fences for GNSS applications," *IEEE Antennas and Wireless Propagation Letters*, Vol. 23, No. 5, 1528–1532, 2024.

[10] Yang, W. J., Y. M. Pan, and S. Y. Zheng, "A low-profile wideband circularly polarized crossed-dipole antenna with wide axial-ratio and gain beamwidths," *IEEE Transactions on Antennas and Propagation*, Vol. 66, No. 7, 3346–3353, 2018.

[11] Nguyen, T. K., H. H. Tran, and N. Nguyen-Trong, "A wideband dual-cavity-backed circularly polarized crossed dipole antenna," *IEEE Antennas and Wireless Propagation Letters*, Vol. 16, 3135–3138, 2017.

[12] Feng, Y., J. Li, B. Cao, J. Liu, G. Yang, and D.-J. Wei, "Cavity-backed broadband circularly polarized cross-dipole antenna," *IEEE Antennas and Wireless Propagation Letters*, Vol. 18, No. 12, 2681–2685, 2019.

[13] Feng, G., L. Chen, X. Wang, X. Xue, and X. Shi, "Broadband circularly polarized crossed bowtie dipole antenna loaded with parasitic elements," *IEEE Antennas and Wireless Propagation Letters*, Vol. 17, No. 1, 114–117, 2018.

[14] Wu, R., J.-H. Lin, J.-F. Li, and F.-C. Chen, "Wideband circularly polarized antenna with novel asymmetric Y-shaped arms," *IEEE Antennas and Wireless Propagation Letters*, Vol. 23, No. 4, 1181–1185, 2024.

[15] Yang, W. J., P. F. Hu, and X. Dai, "A filtering, wideband circularly polarized crossed-dipole antenna," *IEEE Transactions on Antennas and Propagation*, Vol. 73, No. 11, 9583–9588, 2025.

[16] Zhou, Q. and X. Ren, "An ultrawideband circularly polarized antenna with traveling-wave loop," *IEEE Antennas and Wireless Propagation Letters*, Vol. 23, No. 8, 2331–2335, 2024.

[17] Cheng, J., Z. Chen, and S. Xu, "A low-profile circularly polarized cross-dipole antenna with AMC reflector," in *2024 IEEE 12th Asia-Pacific Conference on Antennas and Propagation (APCAP)*, 1–2, Nanjing, China, 2024.

[18] Qiu, L. and G. Xiao, "An artificial magnetic conductor-based wideband circularly polarized antenna with low-profile and enhanced gain," *Electronics*, Vol. 10, No. 17, 2121, 2021.

[19] Xu, R., S. S. Gao, J. Liu, J.-Y. Li, Q. Luo, W. Hu, L. Wen, X.-X. Yang, and J. T. S. Sumantyo, "Analysis and design of ultrawideband circularly polarized antenna and array," *IEEE Transactions on Antennas and Propagation*, Vol. 68, No. 12, 7842–7853, 2020.

[20] Chen, Z., J. Cheng, S. Xu, and W. Wang, "Ultra-wideband low-profile circularly polarized cross-dipole antenna with hybrid AMC reflector," *IEEE Antennas and Wireless Propagation Letters*, Vol. 24, No. 9, 3278–3282, 2025.

[21] Zhou, X., J. Shi, D. Feng, and H. Zhai, "A low-profile dual-polarized MIMO antenna array with high isolation," in *2018 International Conference on Microwave and Millimeter Wave Technology (ICMMT)*, 1–3, Chengdu, China, 2018.

[22] Jiang, Z., Z. Wang, L. Nie, X. Zhao, and S. Huang, "A low-profile ultrawideband slotted dipole antenna based on artificial magnetic conductor," *IEEE Antennas and Wireless Propagation Letters*, Vol. 21, No. 4, 671–675, 2022.